Thermoelectric Performance of the 2D $Bi_2Si_2Te_6$ Semiconductor

Yubo Luo,[†] Zheng Ma,[†] Shiqiang Hao,[#] Songting Cai,[#] Zhong-Zhen Luo,[‡] Christopher Wolverton,[#] Vinayak P. Dravid,[#] Junyou Yang*[,†], Qingyu Yan,*[,‡] Mercouri G. Kanatzidis*[,§]

[†]State Key Laboratory of Materials Processing and Die & Mould Technology, School of Materials Science and Engineering, Huazhong University of Science and Technology, Wuhan, 430074 P. R. China

E-mail: jyyang@mail.hust.edu.cn

[‡]School of Materials Science and Engineering, Nanyang Technological University, 50 Nanyang Avenue, Singapore 639798, Singapore.

E-mail: AlexYan@ntu.edu.sg

[§]Department of Chemistry, Northwestern University, Evanston, Illinois 60208, United States.

E-mail: m-kanatzidis@northwestern.edu

[#] Department of Materials Science and Engineering, Northwestern University, Evanston, Illinois 60208, United States.

KEYWORDS. $Bi_2Si_2Te_6$, $Sb_2Si_2Te_6$, thermoelectric, thermal conductivity, Seebeck coefficient.

ABSTRACT: $Bi_2Si_2Te_6$, a 2D compound, is a direct band gap semiconductor with an optical band gap of 0.25 eV, and is a promising thermoelectric material. Single-phase $Bi_2Si_2Te_6$ is prepared by a scalable ball-milling and annealing process and the highly densified polycrystalline samples are prepared by spark plasma sintering. $Bi_2Si_2Te_6$ shows a p-type semiconductor transport behavior and exhibits an intrinsically low lattice thermal conductivity of ~0.48 $Wm^{-1}K^{-1}$ (cross-plane) at 573 K. The first-principles density functional theory calculations indicate that such low lattice thermal conductivity is derived from the interactions between acoustic phonons and low-lying optical phonons, local vibrations of Bi, the low Debye temperature and strong anharmonicity result from the unique 2D crystal structure and metavalent bonding of $Bi_2Si_2Te_6$. The $Bi_2Si_2Te_6$ exhibits an optimal figure of merit ZT of ~0.51 at 623 K, which can be further enhanced by the substitution of Bi with Pb. Pb doping leads to a large increase in power factor $S^2\sigma$, from ~4.0 $\mu Wcm^{-1}K^{-2}$ of $Bi_2Si_2Te_6$ to ~8.0 $\mu Wcm^{-1}K^{-2}$ of $Bi_{1.98}Pb_{0.02}Si_2Te_6$ at 775 K, owing to the increase in carrier concentration. Moreover, Pb doping induces a further reduction in the lattice thermal conductivity to ~0.38 $Wm^{-1}K^{-1}$ (cross-plane) at 623 K in $Bi_{1.98}Pb_{0.02}Si_2Te_6$,. The simultaneous optimization of the power factor and lattice thermal conductivity achieves a peak ZT of ~0.90 at 723 K and a high average ZT of ~0.66 at 400–773 K in $Bi_{1.98}Pb_{0.02}Si_2Te_6$.

■ INTRODUCTION

The thermoelectric energy conversion technology is of importance in increasing energy efficiency as it allows the direct conversion of heat energy to electricity,[1-3] thus lots of thermoelectric generator prototypes have been developed using bismuth antimony telluride, GeTe, PbTe, half Heuslers, silicides, SnSe and so on in recent years.[4-9] To generate power efficiently from heat, it is desirable that the thermoelectric materials employed in generator have high dimensionless figure of merit (ZT), expressed as $ZT = S^2\sigma T/\kappa$, where S is the Seebeck coefficient, σ is the electrical conductivity, T is the absolute temperature, κ is the thermal conductivity ($S^2\sigma$ is referred to as the power factor).[10-15] High energy conversion efficiency requires high ZT, which in turn requires either high $S^2\sigma$ or low κ.[16] Therefore, to achieve high thermoelectric performance, ongoing efforts in thermoelectric research are focused on the exploration of materials with intrinsically low thermal conductivity,[17] such as Mg_3Sb_2,[18] $SnSe_2$,[19] BiCuSeO,[20] $Cu_{12}Sb_4S_{13}$,[21] Cu_2S,[22] AgCuTe,[23] SnSe,[24-28] $AgGaTe_2$,[29] $CuSbSe_2$,[30, 31] and $AgSbTe_2$[1]. Interestingly, many of these compounds have a 2D layered crystal structure with anharmonic and weak interlayer chemical bonding (e.g. van der Waals bonding).[3]

Recently, we demonstrated that $Sb_2Si_2Te_6$ with a 2D layered structure is a potential p-type high-performance thermoelectric material,[32, 33] it exhibits a peak ZT of ~1.08 at 823 K. $Bi_2Si_2Te_6$[34-36] is an analog of $Sb_2Si_2Te_6$, which also crystallizes in the same rhombohedral symmetry (space group $R\bar{3}$

) with three crystallographic positions [Bi(6c), Si(6c), and Te(18d)]. Single-crystal $Bi_2Si_2Te_6$ was grown via chemical vapor deposition in approximately two months, and was reported to exhibit an inherently low lattice thermal conductivity (~0.84 $Wm^{-1}K^{-1}$ at 320 K) and moderate Seebeck coefficient (~120 μVK^{-1} at 320 K), which is similar to that of $Sb_2Si_2Te_6$.[32] However, the electrical conductivity of $Bi_2Si_2Te_6$ is only ~106 S/cm at 320 K, about one-fifth of $Sb_2Si_2Te_6$, resulting in a low value of peak ZT (~0.12) at 500 K. The development of convenient preparation processes of high-quality samples will promote further investigation of the properties and thermoelectric performance of $Bi_2Si_2Te_6$.

Herein, we report a scalable and efficient method to prepare bulk quantities of single-phase polycrystalline $Bi_2Si_2Te_6$ through ball-milling and annealing. Densified $Bi_2Si_2Te_6$ pellets are obtained by spark plasma sintering (SPS). They exhibit the p-type electrical transport behavior, a low lattice thermal conductivity [~0.48 $Wm^{-1}K^{-1}$ (cross-plane) at 573 K], and a peak ZT value of 0.51 (cross-plane) at 623 K. We confirm that $Bi_2Si_2Te_6$ is a direct band gap semiconductor with an optical band gap of ~0.25 eV. Our density functional theory (DFT) calculations reveal that the intrinsically low lattice thermal conductivity mainly resulted from the interactions between acoustic phonons and low-lying optical phonons, low Debye temperature, and strong anharmonicity in $Bi_2Si_2Te_6$. Furthermore, we reveal that Bi substitution with Pb enhances the hole carrier concentration and power factor of $Bi_2Si_2Te_6$, and further suppresses heat propagation in $Bi_2Si_2Te_6$, owing to the strengthened point defect phonon scattering. Consequently, the simultaneous optimization of electrical and thermal transport properties through Pb doping achieves a peak ZT of ~0.90 (cross-plane) at 723 K for $Bi_{1.98}Pb_{0.02}Si_2Te_6$.

■ RESULTS AND DISCUSSION

1. Crystal structure, band structure and microstructure

2D $Bi_2Si_2Te_6$ is isostructural to $Sb_2Si_2Te_6$ and crystallizes in rhombohedral symmetry space group $R\bar{3}$, with the lattice parameters of a = 7.265(1) Å and c =21.280(2) Å, as shown in Figure 1 a, b. $Bi_2Si_2Te_6$ has a layered structure similar to that of $Fe_2P_2Se_6$,[37] in which one-third of the cation sites are occupied by Si–Si dimers, and Bi^{3+} ions form a honeycomb lattice in the *ab* plane. $Bi_2Si_2Te_6$ layers stack along the *c*-axis (Figure 1a), with an interlayer distance of ~3.92 Å, which is commonly called as van der Waals gap. However, it is also noted that the interatomic distance in $Bi_2Si_2Te_6$ is shorter than the sum of the van der Waals radii of two Te atoms (~4.12 Å),[38] indicating a stronger coupling across the gap than the theoretical one of a common Te-Te van der Waals bonding. Such an unconventional bonding has been recently regarded as 'metavalent bonding',[39-41] which has been observed in several chalcogenides, including layered V_2VI_3 compounds (Bi_2Te_3, Bi_2Se_3, Sb_2Te_3, and β-As_2Te_3), [42] GeTe,[42] GeSe,[43] SnTe[44] and so on. The metavalent bonding is expected to create large Born effective charge, unique atomic vibration property, high lattice anharmonicity (large Grüneisen parameter), high Seebeck coefficient, high optical dielectric constant and low lattice thermal conductivity,[42-44] thus favorable for thermoelectric materials. Polycrystalline $Bi_2Si_2Te_6$ samples were synthesized by a ball-milling and annealing method [see experimental details in the Supporting Information (SI)]. Our Rietveld refinement of the powder X-ray diffraction (XRD) patterns (Figure 1c) confirms the formation of single-phase $Bi_2Si_2Te_6$ (rhombohedral, a = 7.270(8) Å and c = 21.343(3) Å), which agrees well with the theoretically simulated single crystal data (ICSD collection code. 195338). $Bi_2Si_2Te_6$ powders have plate-like non-uniform grain size distribution; the size ranges from hundreds of nanometers to several micrometers (Figure S1 in the SI).

DFT calculations (Figure 1d) and electronic absorption spectroscopic characterization results (Figure S2 in the SI) reflect that $Bi_2Si_2Te_6$ is a direct bandgap semiconductor with a narrow optical band gap E_g of ~0.25 eV, much lower than that of $Sb_2Si_2Te_6$ (~0.60 eV).[32] It is noted that the DFT predicted band gap is lower than the optical one due to the inadequate description of the electronic properties by DFT. In addition, the density of states effective masses (m_d^*) for electrons and holes were found to be ~0.14 m_0 and ~0.16 m_0 (m_0 is the free-electron effective mass) by fitting the band structure around the conduction band minimum and valence band maximum using the following equation: $m^* = \hbar^2/(d^2E/dk^2)$, respectively. The m_d^* of $Bi_2Si_2Te_6$ was smaller than that of $Sb_2Si_2Te_6$, which possesses the m_d^* values of ~0.36 m_0 and ~0.66 m_0 for electrons and holes respectively.[32] Pb-doped $Bi_2Si_2Te_6$ samples ($Bi_{2-x}Pb_xSi_2Te_6$, x=0.01, 0.02, 0.03 and 0.04) were also prepared using the ball-milling and annealing process. The Bragg peaks (Figure 1e) for all the Pb-doped $Bi_2Si_2Te_6$ samples were well indexed to the trigonal $Bi_2Si_2Te_6$ (ICSD collection code. 195338), while an enhanced relative intensity of {01$\bar{1}$} facets was observed in the Pb-doped $Bi_2Si_2Te_6$ than pure one because of the formation of nanoscale grains as we discussed below.

Figure 2 shows the field emission scanning electron microscopy (FESEM) images of $Bi_{2-x}Pb_xSi_2Te_6$ pellets (x=0, 0.02, and 0.04) obtained by SPS. The pellets are composed of randomly arranged flake clusters, whose average grain size gradually decreases, from ~20 μm in pristine $Bi_2Si_2Te_6$ to ~10 μm for $Bi_{1.96}Pb_{0.04}Si_2Te_6$ (Figures 2a–f). Moreover, even nanoscale grains were readily observed in the $Bi_{1.96}Pb_{0.04}Si_2Te_6$ sample (Figures S3 in the SI), indicating that Pb doping possibly suppresses the atomic diffusion and grain boundary movement during the recrystallization process of $Bi_2Si_2Te_6$, thus curbing the enlarging of grain size. The nanograins were characterized by scanning transmission electron microscopy (STEM) (Figure 3a) coupled with energy-dispersive X-ray spectroscopy (EDXS, Figure 3b). Bi, Si, Pb and Te were found to distribute uniformly in $Bi_{1.96}Pb_{0.04}Si_2Te_6$, without obvious compositional differences between the nanograin and adjacent microscale grains. The XRD, FESEM and transmission electron microscopy (TEM) results indicated that Pb doping can reduce the grain size of $Bi_2Si_2Te_6$, but allows the maintenance of its crystal structure and phase.

In addition, we performed TEM of a separated flake for $Bi_{1.98}Pb_{0.02}Si_2Te_6$ obtained by ultrasonic dispersion (Figure 3c). We observed that the flake constituted of several plates (Figure 3d) with nanoscale thickness, which is in good agreement with the FESEM results (Figure 2). The corresponding selected area electron diffraction (SAED) pattern (inset of Figure 3e) of the multiple plates zone exhibits a clear rhombohedral symmetric Bragg spot pattern indexed to $Bi_2Si_2Te_6$ (space group $R\bar{3}$) along the [001] zone axis. This indicates that the $Bi_2Si_2Te_6$ flake grows laterally along its ab plane during SPS process, since the obtained powders are irregular (Figure S1 in the SI). In addition, the results of high-resolution TEM images (Figure 3f, g) also indicate that the nanoplates are single-crystallized and have the same growth orientation (i.e., along ab plane) in the single flake.

2. Thermoelectric properties

Figure 4 shows the thermoelectric properties of the $Bi_{2-x}Pb_xSi_2Te_6$ pellets (x = 0, 0.01, 0.02, 0.03, and 0.04) and $Sb_2Si_2Te_6$ (for comparison). Considering the possible anisotropy that can originate from the lamellar morphology of the grains and the layered crystal structure, we measured the electrical and thermal transport properties in two directions: perpendicular to the SPS pressure (mostly in-plane direction) and parallel to the SPS pressure (mostly cross-plane direction) (see Figure S4 in the SI). In general, the electrical conductivity of $Bi_2Si_2Te_6$ along the in-plane direction (~ 88.8 S/cm) is slightly higher than that along the cross-plane direction (64.2 S/cm) at room temperature. The electrical conductivity of $Bi_2Si_2Te_6$ reveals its semiconductor behavior and increases with temperature in the range of 310–473 K. The activation energy[19] is estimated to be ~0.03 eV. After 473 K, the electrical conductivity gradually decreases to a minimum value, i.e., 88.9 S/cm (in-plane) and 77.5 S/cm (cross-plane) at 673 K, and then slightly increases due to the rise in the thermally activated carrier concentration induced by intrinsic excitation.

The Seebeck coefficients of $Bi_2Si_2Te_6$ are positive (reflecting its p-type transport nature), and increases from 122 μVK^{-1} (in-plane) or 124 μVK^{-1} (cross-plane) at 310 K to a maximum of 229 μVK^{-1} (in-plane) or 237 μVK^{-1} (cross-plane) at 623 K, Figure 4b. Above this temperature, the onset of intrinsic excitation (i.e., bipolar conduction) is observed, causing a decrease to 199 μVK^{-1} (in-plane) or 201 μVK^{-1} (cross-plane) at 773 K, similar to other semiconductors (e.g., Bi_2Te_3,[4, 5] In_4Se_{3-x}[45] and MgAgSb[46]) with a narrow band gap. It is noted that the Goldsmid–Sharp band gap is ~0.29 eV, estimated using the maximum value Seebeck coefficient ($E_g=2eS_{max}T_{max}$),[45] which is consistent with the optically measured one (~0.25 eV, Figure S2 in the SI).

The Seebeck coefficients of $Bi_2Si_2Te_6$ are slightly higher than its analog $Sb_2Si_2Te_6$ at 310–723 K, as shown in Figure 4b. However, the electrical conductivity of $Bi_2Si_2Te_6$ is much lower than that of $Sb_2Si_2Te_6$ over the entire temperature range of measurements (i.e., 310–773 K). For instance, the room-temperature electrical conductivity is 531.9 S/cm (in-plane) or 510.0 S/cm (cross-plane) for $Sb_2Si_2Te_6$, which is almost six (in-plane) to eight (cross-plane) times higher than that of $Bi_2Si_2Te_6$. Hall effect measurements (Figure S5) show that the Hall mobility for $Bi_2Si_2Te_6$ is 57 $cm^2V^{-1}s^{-1}$ (in-plane) or 51 $cm^2V^{-1}s^{-1}$ (cross-plane) at room temperature, which is only slightly lower than that of $Sb_2Si_2Te_6$ [i.e., 60 $cm^2V^{-1}s^{-1}$ (in-plane) or 59 $cm^2V^{-1}s^{-1}$ (cross-plane)].[31] However, the room-temperature carrier concentration of $Bi_2Si_2Te_6$ is 9.8 × 10^{18} cm^{-3} (in-plane) or 7.9 × 10^{18} cm^{-3} (cross-plane), which is much lower than that of $Sb_2Si_2Te_6$ [i.e., 5.6 × 10^{19} cm^{-3} (in-plane) or 5.4 × 10^{19} cm^{-3} (cross-plane) arises from Sb vacancies].[32] The lower carrier concentration of $Bi_2Si_2Te_6$ is the main reason for its lower electrical conductivity than that of $Sb_2Si_2Te_6$. The low electrical conductivity of $Bi_2Si_2Te_6$ leads to low power factor $S^2\sigma$ of ~3.9 $\mu Wcm^{-1}K^{-2}$ (in-plane) or ~3.4 $\mu Wcm^{-1}K^{-2}$ (cross-plane) at 773 K, which is approximately one-third that of $Sb_2Si_2Te_6$, as shown in Figure 4c. Therefore, it is important to enhance the hole concentration to increase the electrical conductivity of $Bi_2Si_2Te_6$.

Inspired by this, the substitution of Bi sites with Pb was carried out to create hole carriers, because of the hole donating nature of Bi, as follows:

$$Pb \xrightarrow{Bi_2Si_2Te_6} Pb_{Bi}^{'}+h^{\cdot} \quad (1)$$

As a result, the hole carrier concentration of $Bi_{1.96}Pb_{0.04}Si_2Te_6$ (i.e., x=0.04) increased to ~9.7×10^{19} cm^{-3} at room temperature, which is an increase of one order of magnitude compared to that of $Bi_2Si_2Te_6$ and also considerably higher than that of $Sb_2Si_2Te_6$. The Hall mobility, however, reduced upon Pb doping, owing to the enhanced scattering of holes by induced point defects Pb_{Bi}'. While the room-temperature Hall mobility of $Bi_{1.96}Pb_{0.04}Si_2Te_6$ reduced slightly owing to the enhanced carrier scattering by Pb_{Bi}', which is 40 $cm^2V^{-1}s^{-1}$ (in-plane) or 37 $cm^2V^{-1}s^{-1}$ (cross-plane).

Because of the large enhancement in carrier concentration, the electrical conductivity of $Bi_2Si_2Te_6$ is significantly enhanced by Pb doping, as shown in Figure 4a. Specifically, the electrical conductivity is 292.9 S/cm (in-plane) or 250.8 S/cm (cross-plane), 468.2 S/cm (in-plane) or 421.5 S/cm (cross-plane), 559.5 S/cm (in-plane) or 528.3 S/cm (cross-plane), and 620.1 S/cm (in-plane) or 582.9 S/cm (cross-plane) at 310 K for $Bi_{1.99}Pb_{0.01}Si_2Te_6$, $Bi_{1.98}Pb_{0.02}Si_2Te_6$, $Bi_{1.97}Pb_{0.03}Si_2Te_6$, and $Bi_{1.96}Pb_{0.04}Si_2Te_6$, respectively. In addition, the electrical conductivity of $Bi_{2-x}Pb_xSi_2Te_6$ (x = 0.01, 0.02, 0.03, and 0.04) decreases monotonically with increasing temperature, which is representative of the typical heavily doped semiconductor behavior.

The Seebeck coefficients of $Bi_2Si_2Te_6$ gradually decreases with increasing amount of doped Pb (Figure 4b), which is consistent with the increase in the carrier concentration, as given by Mott expression.[45] For example, the room-temperature Seebeck coefficients of $Bi_{1.99}Pb_{0.01}Si_2Te_6$, $Bi_{1.98}Pb_{0.02}Si_2Te_6$, $Bi_{1.97}Pb_{0.03}Si_2Te_6$ and $Bi_{1.96}Pb_{0.04}Si_2Te_6$ are 121 μVK^{-1} (in-plane) or 114 μVK^{-1} (cross-plane), 91 μVK^{-1} (in-plane) or 94 μVK^{-1} (cross-plane), 75 μVK^{-1} (in-plane) or 74 μVK^{-1} (cross-plane), and 69 μVK^{-1} (in-plane) or 69 μVK^{-1} (cross-plane), respectively. In addition, the Seebeck coefficients of Pb-doped samples increase with the rising temperature from 310 K to 773 K, also indicating the heavily doped semiconductor behavior.

Derived from the measured electrical conductivities and Seebeck coefficients, the temperature-dependent thermoelectric power factors of $Bi_{2-x}Pb_xSi_2Te_6$ (x=0, 0.01, 0.02, 0.03 and 0.04) are depicted in Figure 4c. In comparison with pristine $Bi_2Si_2Te_6$, Pb-doped samples exhibit considerably higher power factors at 300–773 K because of the considerable increase in electrical conductivity. Especially, the $S^2\sigma$ of

$Bi_{1.97}Pb_{0.03}Si_2Te_6$ (x = 0.03) reaches 8.3 μWcm^{-1}K^{-2} (in-plane) or 8.9 μWcm^{-1}K^{-2} (cross-plane) at 773 K, which is more than twice that of pure $Bi_2Si_2Te_6$ [3.9 μWcm^{-1}K^{-2} (in-plane) or 3.4 μWcm^{-1}K^{-2} (cross-plane)]. More importantly, such high $S^2\sigma$ of $Bi_{1.97}Pb_{0.03}Si_2Te_6$ is close to that of $Sb_2Si_2Te_6$ [9.9 μWcm^{-1}K^{-2} (in-plane) or 9.7 μWcm^{-1}K^{-2} (cross-plane)], indicating that the substitution of Bi sites with Pb is highly effective in enhancing the electrical transport properties of $Bi_2Si_2Te_6$.

The thermal conductivity of pristine $Bi_2Si_2Te_6$ (Figure 4d) along the in-plane direction is also slightly higher than that along the cross-plane direction, which is ~1.06 Wm^{-1}K^{-1} (in-plane) or ~0.89 Wm^{-1}K^{-1} (cross-plane) at 310 K, respectively. With increasing temperature, the thermal conductivity decreases to a minimum value of ~0.67 Wm^{-1}K^{-1} (in-plane) or ~0.57 Wm^{-1}K^{-1} (cross-plane) at 623 K as lattice vibration increases with rising temperature, and then increases to ~0.76 Wm^{-1}K^{-1} (in-plane) or ~0.64 Wm^{-1}K^{-1} (cross-plane) at 773 K as bipolar conduction process occurs.

The electronic contribution to the total thermal conductivity is commonly evaluated using the Wiedemann–Franz law: electronic contribution $\kappa_e = LT\sigma$, wherein L is the Lorenz number and evaluated by an empirical formula L = 1.5+exp(-|S|/116).[47] The corresponding results are plotted in Figure S6. The lattice thermal conductivities, κ_L, obtained by subtracting κ_e from total κ, are shown in Figure 4e. It is observed that the κ_L of $Bi_2Si_2Te_6$ is very low (<1 Wm^{-1}K^{-1}) over 300–773 K. It decreases from ~1.01 Wm^{-1}K^{-1} (in-plane) or ~0.85 Wm^{-1}K^{-1} (cross-plane) at 310 K to the minimum value of ~0.56 Wm^{-1}K^{-1} (in-plane) or ~0.48 Wm^{-1}K^{-1} (cross-plane) at 573 K, and then increases up to ~0.63 Wm^{-1}K^{-1} (in-plane) or ~0.53 Wm^{-1}K^{-1} (cross-plane) at 773 K due to the sizable heat propagation induced by the well-known bipolar effect. This intrinsically low lattice thermal conductivity of $Bi_2Si_2Te_6$ is even lower than that of $Sb_2Si_2Te_6$ [whose minimum κ_L is ~0.51 Wm^{-1}K^{-1} (in-plane) or ~0.48 Wm^{-1}K^{-1} (cross-plane) at 823 K], as well as the well-established thermoelectrical materials (e.g., $CoSb_3$,[48] SnTe,[49, 50] PbS,[51, 52] PbTe,[53, 54] and half-Heusler[55]). Therefore, $Bi_2Si_2Te_6$ is applicable as a thermoelectric material.

Upon Pb doping, the overall thermal conductivity of $Bi_2Si_2Te_6$ increases over the whole measured temperature range (Figure 4d) because of the enhancement of the electronic thermal conductivity. For example, the thermal conductivities of $Bi_{1.99}Pb_{0.01}Si_2Te_6$, $Bi_{1.98}Pb_{0.02}Si_2Te_6$, $Bi_{1.97}Pb_{0.03}Si_2Te_6$, and $Bi_{1.96}Pb_{0.04}Si_2Te_6$ are ~1.30 (in-plane) or ~1.11 Wm^{-1}K^{-1} (cross-plane), ~1.21 (in-plane) or ~1.20 Wm^{-1}K^{-1} (cross-plane), ~1.77 (in-plane) or ~1.53 Wm^{-1}K^{-1} (cross-plane), and ~1.80 (in-plane) or ~1.56 Wm^{-1}K^{-1} (cross-plane) at 310 K, respectively.

In addition, the already low lattice thermal conductivity of $Bi_2Si_2Te_6$ further slightly decreases upon Pb doping (Figure 4e). Because the atomic mass and radius for Pb and Bi are very close and the micro-scale average grain size, the influence of point defect (Pb_{Bi}') and grain-boundary phonon scattering is marginal. We attribute the reduction in lattice thermal conductivity to the extra phonon scattering by nano-grains and the enhanced electron-phonon interaction[56] caused by the largely enhanced carrier concentration in Pb doped $Bi_2Si_2Te_6$. In which, $Bi_{1.98}Pb_{0.02}Si_2Te_6$ was found to exhibit the lowest lattice thermal conductivity of ~0.43 Wm^{-1}K^{-1} (in-plane) or ~0.38 Wm^{-1}K^{-1} (cross-plane) at 623 K in $Bi_{2-x}Pb_xSi_2Te_6$ system, which is comparable with thermoelectric materials with ultralow lattice thermal conductivities, such as $Rb_2Bi_8Se_{13}$,[57] $AgBi_3S_5$,[58] Ag_9AlSe_6,[59] and AgCuTe.[23] In addition, the bipolar thermal conductivity of $Bi_2Si_2Te_6$ was suppressed by Pb doping in the intrinsic conduction region (573–773 K), especially of $Bi_{1.97}Pb_{0.03}Si_2Te_6$ and $Bi_{1.96}Pb_{0.04}Si_2Te_6$. We attributed it to the largely enhanced hole concentration, as observed in other narrow band gap semiconductors.[60, 61]

Figure 4f shows the temperature-dependent ZT values of $Bi_{2-x}Pb_xSi_2Te_6$ (x = 0, 0.01, 0.02, 0.03, and 0.04). $Bi_2Si_2Te_6$ exhibits the optimal ZT value of 0.49 (in-plane) or 0.51 (cross-plane) at 623 K, which gradually reduces to 0.40 (in-plane) or 0.42 (cross-plane) at 773 K, respectively. The ZT value of $Bi_2Si_2Te_6$ is lower than that of $Sb_2Si_2Te_6$, whose optimal ZT value is 1.05 (in-plane) or 1.08 (cross-plane) at 823 K. We ascribe the decrease in ZT to the lower electrical conductivity of $Bi_2Si_2Te_6$ than $Sb_2Si_2Te_6$ caused by its low carrier concentration, and the higher thermal conductivity of $Bi_2Si_2Te_6$ than $Sb_2Si_2Te_6$ caused by intrinsic excitation. Subsequently, significant enhancement of the electrical conductivity and suppression of the bipolar effect were achieved through Pb doping. $Bi_{1.98}Pb_{0.02}Si_2Te_6$ exhibited the highest thermoelectric performance with a peak ZT of 0.80 (in-plane) or 0.90 (cross-plane) at 723 K, almost twice the value of $Bi_2Si_2Te_6$ [e.g., 0.45 (cross-plane) at 723 K]. More importantly, according to the following equation:[62]

$$ZT_{ave} = \frac{1}{T_h - T_c}\int_{T_c}^{T_h} ZT\, dT \qquad (2)$$

where T_h and T_c are the hot-side and cold-side temperatures, respectively. We calculated the average ZT of $Bi_{1.98}Pb_{0.02}Si_2Te_6$, which is ~0.66 along the cross-plane direction at 400–773 K (Figure S7 in the SI), which is ~60% higher than that of pure $Bi_2Si_2Te_6$ (0.41, cross-plane) and nearly equal to that of $Sb_2Si_2Te_6$ (~0.67 in 400–823 K). Such a high average ZT is comparable to those of the well-established PbSe- and SnTe-based thermoelectric materials[63, 64], implying the high potential of Pb-doped $Bi_2Si_2Te_6$ in thermoelectric power generation.

3. Origin of low lattice thermal conductivity

To get a better insight into the intrinsically low lattice thermal conductivity of $Bi_2Si_2Te_6$, we performed first-principles DFT calculations on its phonon dispersion spectrum, **Figure 5a**. The three phonon dispersion branches originate from the Γ-point corresponding to acoustic modes, including two transverse modes (TA and TA′) and a longitudinal mode (LA). Frequency q for these acoustic branches increases toward the Brillouin zone boundaries and saturate at ~18–38 cm^{-1}. At this wavelength, the TA mode shows a quadratic energy dispersion relation, while the TA′ and LA modes show a normal linear dispersion near the Γ point, which is in accordance with the structural properties of $Bi_2Si_2Te_6$. In addition, we noted many soft (low-lying) optical modes in this compound, especially at the zone center (Γ point), with frequency as low as ~17 cm^{-1}, even much lower than that observed in $Sb_2Si_2Te_6$ (~25 cm^{-1}). These soft optical modes overlap with the acoustic branches, leading to strong mixing and highly nonlinear dispersion curves away from the center of the Brillouin zone. The atom-projected phonon DOS in Figure 5b shows that the low-frequency optical modes at the Brillouin zone center are dominant contributions from the local vibrations of Bi ions, followed by Te ions in the distorted [$BiTe_6$] octahedral (Figure S8 in the SI). The interactions between acoustic phonons and low-lying optical phonons are conducive to low lattice thermal conductivity.[65, 66]

The longitudinal Debye temperature (θ_D) and phonon velocity for these acoustic modes, evaluated on the basis of the acoustic phonon dispersion, are 40 K and 2035 m/s, 45 K and 2149 m/s, and 48 K and 2070 m/s along the Γ−Z, Γ−X, and Γ−L directions, respectively. Such low Debye temperature values indicate a high density of low energy phonons and weak atomic bonding in $Bi_2Si_2Te_6$. In addition, we plotted the dispersion of the Grüneisen parameters in $Bi_2Si_2Te_6$ to quantitatively estimate the strength of the anharmonicity; the plots are shown in Figure 5c. The Grüneisen parameters (γ) for the TA mode of $Bi_2Si_2Te_6$ is higher than 6 at Γ point, which is comparable with that of $Sb_2Si_2Te_6$; while the γ for the TA′ and LA modes of $Bi_2Si_2Te_6$ are lower than 2 at Γ point, lower than that of $Sb_2Si_2Te_6$ ($\gamma_{TA'}$ ~5, γ_{LA} ~ 6 at Γ point).[32] It indicates the TA mode is highly anharmonic and interacts strongly with other acoustic phonons in $Bi_2Si_2Te_6$. This behavior originates from the out-of-plane vibration of Bi and Te atoms (Figure 4b). The low Debye temperature (<50 K) and strong anharmonicity (i.e., the large Grüneisen parameters) are also able to account for the low lattice thermal conductivity of $Bi_2Si_2Te_6$, as observed in other thermoelectric materials,[66, 67] according to the following equation:

$$\kappa_L = \frac{MV^{1/3}\theta_D^3}{\gamma^2 T} \tag{3}$$

where M and V are the average atomic mass and average atomic volume, respectively. Fundamentally, the low-lying optical phonons, low Debye temperature, large anharmonicity, and high Grüneisen parameters (γ) for the TA mode further reflect the existence of so-called metavalent bonding in $Bi_2Si_2Te_6$, which is expected to induce ultralow lattice thermal conductivities. [39-44] Therefore, we further calculated the lattice thermal conductivities using the Debye−Callaway formalism[68] along the a-, b-, and c-axes, respectively, as well as the average lattice thermal conductivities (Figure 5d). In particular, the average lattice thermal conductivity of $Bi_2Si_2Te_6$ is 1.77 $Wm^{-1}K^{-1}$ at 300 K, which falls to an ultralow value of 0.63 $Wm^{-1}K^{-1}$ at 800 K (see lattice thermal conductivity calculations in the SI). Our DFT calculations reflect the significant contribution of the interactions between acoustic phonons and low-lying optical phonons, low Debye temperature, and strong anharmonicity caused by so-called mentavalent bonding toward the low lattice thermal conductivity.

■ CONCLUDING REMARKS

This work reported a scalable ball-milling and annealing method to synthesize the 2D $Bi_2Si_2Te_6$ semiconductor. DFT calculations showed that $Bi_2Si_2Te_6$ has strong interactions between acoustic phonons and low-lying optical phonons, low Debye temperature, and strong anharmonicity. These features enable $Bi_2Si_2Te_6$ to have a low lattice thermal conductivity of ~0.56 $Wm^{-1}K^{-1}$ (in-plane) or ~0.48 $Wm^{-1}K^{-1}$ (cross-plane) at 573 K, even lower than those of its analog $Sb_2Si_2Te_6$ at the same temperature. Moreover, the electron accepting nature of Bi atoms upon Pb doping leads to a large increase in hole concentration and promotes the transition to degenerate transport behavior that enhances the power factors. The cross-plane power factor reaches to 7.6 μ$Wcm^{-1}K^{-2}$ (in-plane) or 8.0 μ$Wcm^{-1}K^{-2}$ (cross-plane) at 773 K for $Bi_{1.97}Pb_{0.03}Si_2Te_6$, which is more than twice the values of $Bi_2Si_2Te_6$. The enhanced power factor and low thermal conductivity allowed the achievement of a peak ZT of ~0.90 at 723 K and a high average ZT of ~0.66 at 400–773 K in $Bi_{1.98}Pb_{0.02}Si_2Te_6$. It was noted that the high average ZT is almost equal to that of $Sb_2Si_2Te_6$ and comparable to those of PbSe- and SnTe-based thermoelectric materials, implying that $Bi_2Si_2Te_6$ is a highly promising new thermoelectric material. Furthermore, the smaller effective masses of electrons and hole carriers predicted by the DFT calculations and direct energy gap of this material suggest additional interesting physical properties such as topological behavior and radiation detection.

■ ASSOCIATED CONTENT

Supporting Information

Experimental and computational details, including FESEM images for $Bi_{2-x}Pb_xSi_2Te_6$ (x=0, 0.01, 0.02, 0.03 and 0.04) powders, Fourier transform infrared spectroscopy of $Bi_2Si_2Te_6$, Hall carrier concentrations and mobilities, electronic thermal conductivities, average ZT values and distorted [$BiTe_6$] octahedra, Figures S1−S9.

■ AUTHOR INFORMATION

Corresponding Author

Junyou Yang

State Key Laboratory of Materials Processing and Die & Mold Technology, Huazhong University of Science and Technology, Wuhan, 430074, P. R. China

Email: jyyang@mail.hust.edu.cn

Qingyu Yan

School of Materials Science and Engineering, Nanyang Technological University, 50 Nanyang Avenue, Singapore 639798, Singapore.

Email: AlexYan@ntu.edu.sg

Mercouri G. Kanatzidis

Department of Chemistry, Northwestern University, Evanston, Illinois 60208, United States.

Email: m-kanatzidis@northwestern.edu

Notes

The authors declare no competing financial interest.

■ ACKNOWLEDGMENT

This work was supported by the National Natural Science Foundation of China (Grant Nos. 52002137, 92163211, 51802070 and 51632006), the Department of Energy, Office of Science Basic Energy Sciences under grant DE-SC0014520, DOE Office of Science. This work made use of the EPIC facilities of Northwestern's NUANCE Center, which has received support from the Soft and Hybrid Nanotechnology Experimental (SHyNE) Resource (NSF ECCS-1542205); the MRSEC program (NSF DMR-1121262) at the Materials Research Center; the International Institute for Nanotechnology (IIN); the Keck Foundation; and the State of Illinois, through the IIN. User Facilities are supported by the Office of Science of the U.S. Department of Energy under Contract No. DE-AC02-06CH11357 and DE-AC02-05CH11231. Access to facilities of high-performance computational resources at the Northwestern University is acknowledged. The authors also acknowledge Singapore MOE AcRF Tier 2 under Grant Nos. 2018-T2-1-010, Singapore A*STAR Pharos Program SERC 1527200022, Singapore A*STAR project A19D9a0096, the Fundamental Research Funds for the Central Universities under Grant No. 2021XXJS008 and 2018KFYXKJC002. We gratefully acknowledge the technical assistance from the Analytical and Testing Center of HUST.

■ REFERENCES

(1) Roychowdhury, S.; Ghosh, T.; Arora, R.; Samanta, M.; Xie, L.; Singh, N. K.; Soni, A.; He, J.; Waghmare, U. V.; Biswas, K., Enhanced atomic ordering leads to high thermoelectric performance in $AgSbTe_2$. *Science* **2021,** *371* (6530), 722-727.

(2) Jiang, B.; Yu, Y.; Cui, J.; Liu, X.; Xie, L.; Liao, J.; Zhang, Q.; Huang, Y.; Ning, S.; Jia, B., High-entropy-stabilized chalcogenides with high thermoelectric performance. *Science* **2021,** *371* (6531), 830-834.

(3) Xiao, Y,; L-D, Zhao., Seeking new, highly effective thermoelectrics. Science **2020**, 367 (6483), 1196-1197.

(4) Meroz, O.; Ayoun, D. B.; Beeri, O.; Gelbstein, Y., Development of $Bi_2Te_{2.4}Se_{0.6}$ Alloy for Thermoelectric Power Generation Applications, *J. Alloys Compd.* **2016***, 679,* 196.

(5) Madar, N.; Givon, G.; Mogilyansky, D.; Gelbstein, Y., High thermoelectric potential of Bi_2Te_3 alloyed GeTe-rich phases. *J. Appl. Phys.* **2016**, *120*, 035102.

(6) Ayoun, D. B.; Sadia, Y.; Gelbstein, Y., High temperature thermoelectric properties evolution of $Pb_{1-x}Sn_xTe$ based alloys. *J. Alloys Compd.* **2017**, *722*, 33.

(7) Jood, P.; Ohta, M.; Yamamoto, A.; Kanatzidis, M. G., Excessively doped PbTe with Ge-induced nanostructures enables high-efficiency thermoelectric modules. *Joule* **2018,** *2* (7), 1339-1355.

(8) Kang, H. B.; Saparamadu, U.; Nozariasbmarz, A.; Li, W.; Zhu, H.; Poudel, B.; Priya, S., Understanding Oxidation Resistance of Half-Heusler Alloys for in-Air High Temperature Sustainable Thermoelectric Generators, *ACS Appl. Mater. Interfaces* **2020**, *12* (32), 36706.

(9) Qin, B.; Wang, D.; Liu, X.; Qin, Y.; Dong, J.-F.; Luo, J.; Li, J.-W.; Liu, W.; Tan, G.; Tang, X., Momentum and energy multiband alignment enable power generation and thermoelectric cooling. *Science* **2021**, *373* (6554), 556-561.

(10) Biswas, K.; He, J.; Blum, I. D.; Wu, C.-I.; Hogan, T. P.; Seidman, D. N.; Dravid, V. P.; Kanatzidis, M. G., High-performance bulk thermoelectrics with all-scale hierarchical architectures. *Nature* **2012,** *489* (7416), 414.

(11) Pei, Y.; Shi, X.; LaLonde, A.; Wang, H.; Chen, L.; Snyder, G. J., Convergence of electronic bands for high performance bulk thermoelectrics. *Nature* **2011,** *473* (7345), 66.

(6) Shi, X.; Wu, A.; Liu, W.; Moshwan, R.; Wang, Y.; Chen, Z.-G.; Zou, J., Polycrystalline SnSe with extraordinary thermoelectric property via nanoporous design. *ACS nano* **2018,** *12* (11), 11417-11425.

(12) Beretta, D.; Neophytou, N.; Hodges, J. M.; Kanatzidis, M. G.; Narducci, D.; Martin-Gonzalez, M.; Beekman, M.; Balke, B.; Cerretti, G.; Tremel, W., Thermoelectrics: From history, a window to the future. *Mater. Sci. Eng. R Rep.* **2019,** *138*, 100501.

(13) He, J.; Tritt, T. M., Advances in thermoelectric materials research: Looking back and moving forward. *Science* **2017,** *357* (6358).

(14) Tan, G.; Zhao, L.-D.; Kanatzidis, M. G., Rationally designing high-performance bulk thermoelectric materials. *Chem. Rev.* **2016,** *116* (19), 12123-12149.

(15) Zheng, Y.; Luo, Y.; Du, C.; Zhu, B.; Liang, Q.; Hng, H. H.; Hippalgaonkar, K.; Xu, J.; Yan, Q., Designing hybrid architectures for advanced thermoelectric materials. *Mater. Chem. Front.* **2017,** *1* (12), 2457-2473.

(16) Yan, Q.; Kanatzidis, M. G., High-performance thermoelectrics and challenges for practical devices. *Nat. Mater*. **2021**, Doi.org/10.1038/s41563-021-01109-w.

(17) Zheng, Y.; Slade, T. J.; Hu, L.; Tan, X. Y.; Luo, Y.; Luo, Z-Z.; Xu, J.; Yan, Q.; Kanatzidis, M. G.; Defect engineering in thermoelectric materials: what have we learned? *Chem. Soc. Rev.* **2021**, *50*, 9022-9054.

(18) Mao, J.; Zhu, H.; Ding, Z.; Liu, Z.; Gamage, G. A.; Ren, Z., High thermoelectric cooling performance of n-type Mg_3Bi_2-based materials. *Science* **2019**, 365 (6452), 495-498.

(19) Luo, Y.; Zheng, Y.; Luo, Z.; Hao, S.; Du, C.; Liang, Q.; Li, Z.; Khor, K. A.; Hippalgaonkar, K.; Xu, J., n-Type $SnSe_2$ Oriented-Nanoplate-Based Pellets for High Thermoelectric Performance. *Adv. Energy Mater.* **2018,** *8* (8), 1702167.

(20) Zhao, L.-D.; He, J.; Berardan, D.; Lin, Y.; Li, J.-F.; Nan, C.-W.; Dragoe, N., BiCuSeO oxyselenides: new promising thermoelectric materials. *Energy Environ. Sci.* **2014,** *7* (9), 2900-2924.

(21) Suekuni, K.; Tsuruta, K.; Kunii, M.; Nishiate, H.; Nishibori, E.; Maki, S.; Ohta, M.; Yamamoto, A.; Koyano, M., High-performance thermoelectric mineral $Cu_{12-x}Ni_xSb_4S_{13}$ tetrahedrite. *J. Phys. D* **2013,** *113* (4), 043712.

(22) He, Y.; Day, T.; Zhang, T.; Liu, H.; Shi, X.; Chen, L.; Snyder, G. J., High Thermoelectric Performance in Non-Toxic Earth-Abundant Copper Sulfide. *Adv. Mater.* **2014,** *26* (23), 3974-3978.

(23) Roychowdhury, S.; Jana, M. K.; Pan, J.; Guin, S. N.; Sanyal, D.; Waghmare, U. V.; Biswas, K., Soft phonon modes leading to ultralow thermal conductivity and high thermoelectric performance in AgCuTe. *Angew. Chem.* **2018,** *130* (15), 4107-4111.

(24) Zhao, L.-D.; Tan, G.; Hao, S.; He, J.; Pei, Y.; Chi, H.; Wang, H.; Gong, S.; Xu, H.; Dravid, V. P., Uher, C.; Snyder, G. J.; Wolverton, C.; Kanatzidis, M. G., Ultrahigh power factor and thermoelectric performance in hole-doped single-crystal SnSe. *Science* **2016,** *351* (6269), 141-144.

(25) Zhao, L.-D.; Lo, S.-H.; Zhang, Y.; Sun, H.; Tan, G.; Uher, C.; Wolverton, C.; Dravid, V. P.; Kanatzidis, M. G., Ultralow

thermal conductivity and high thermoelectric figure of merit in SnSe crystals. *Nature* **2014,** *508* (7496), 373-377.
(26) Chang, C.; Wu, M.; He, D.; Pei, Y.; Wu, C.-F.; Wu, X.; Yu, H.; Zhu, F.; Wang, K.; Chen, Y., 3D charge and 2D phonon transports leading to high out-of-plane ZT in n-type SnSe crystals. *Science* **2018,** *360* (6390), 778-783.
(27) Lee, Y. K.; Luo, Z.; Cho, S. P.; Kanatzidis, M. G.; Chung, I., Surface oxide removal for polycrystalline SnSe reveals near-single-crystal thermoelectric performance. *Joule* **2019,** *3* (3), 719-731.
(28) Zhou, C.; Lee, Y. K.; Yu, Y.; Byun, S.; Luo, Z-Z.; Lee, H.; Ge, B.; Lee, Y-L.; Chen, X.; Lee, J. Y.; Cojocaru-Mirédin, Chang, H.; Im, J.; Cho, S-P.; Wuttig, M.; Dravid, V. P.; Kanatzidis, M. G.; Chung, I.; Polycrystalline SnSe with a thermoelectric figure of merit greater than the single crystal. *Nat. Mater.* **2021**, 20, 1378-1384.
(29) Su, X.; Zhao, N.; Hao, S.; Stoumpos, C. C.; Liu, M.; Chen, H.; Xie, H.; Zhang, Q.; Wolverton, C.; Tang, X., High Thermoelectric Performance in the Wide Band-Gap $AgGa_{1-x}Te_2$ Compounds: Directional Negative Thermal Expansion and Intrinsically Low Thermal Conductivity. *Adv. Funct. Mater.* **2019,** *29* (6), 1806534.
(30) Luo, Y.; Du, C.; Liang, Q.; Zheng, Y.; Zhu, B.; Hu, H.; Khor, K. A.; Xu, J.; Yan, Q.; Kanatzidis, M. G., Enhancement of Thermoelectric Performance in $CuSbSe_2$ Nanoplate-Based Pellets by Texture Engineering and Carrier Concentration Optimization. *Small* **2018**, 1803092.
(31) Zhang, D.; Yang, J.; Jiang, Q.; Fu, L.; Xiao, Y.; Luo, Y.; Zhou, Z., Ternary $CuSbSe_2$ chalcostibite: facile synthesis, electronic-structure and thermoelectric performance enhancement. *J. Mater. Chem. A* **2016,** *4* (11), 4188-4193.
(32) Luo, Y.; Cai, S.; Hao, S.; Pielnhofer, F.; Hadar, I.; Luo, Z.-Z.; Xu, J.; Wolverton, C.; Dravid, V. P.; Pfitzner, A.; Yan, Q.; Kanatzidis, M. G., High-performance thermoelectrics from cellular nanostructured $Sb_2Si_2Te_6$. *Joule* **2020,** *4* (1), 159-175.
(33) Xu, T.; Haruna, A-Y.; Ma, Z.; Li, W.; Li, J.; Luo, Y.; Zhang, D.; Yang, J., High Power Factor and Thermoelectric Figure of Merit in $Sb_2Si_2Te_6$ through Synergetic Effect of Ca Doping. *Chem. Mater.* **2021**, 33 (20), 8097-8105.
(34) Arabbagheri, S., Präparative Untersuchung an Thermoelektrischen Materialien. *Universität Regensburg* **2015**, DOI: 10.5283/epub.30984
(35) Seidlmayer, S., Strukturchemische Untersuchungen an Hexachalkogenohypodiphosphaten und verwandten Verbindungen. *Universität Regensburg* **2010**, DOI: 10.5283/epub.13427
(36) Fiedler, D., Synthese, Struktur und spektroskopische Eigenschaften selen-und tellurhaltiger topologischer Isolatoren und thermoelektrischer Materialien. *Universität Regensburg* **2019**, DOI: 10.5283/epub.36489.
(37) Klingen, W.; Eulenberger, G.; Hahn, H., Uber die kristallstrukturen von $Fe_2P_2Se_6$ und $Fe_2P_2S_6$. *Zeitschrift für anorganische und allgemeine Chemie* **1973,** *401* (1), 97-112.
(38) Yi, S.; Zhu, Z.; Cai, X.; Jia, Y.; Cho, J-H., The Nature of Bonding in Bulk Tellurium Composed of One-Dimensional Helical Chains. *Inorg. Chem*. **2018**, *57*(9), 5083-5088.
(39) Wuttig, M.; Deringer, V. L.; Gonze, X.; Bichara, C.; Raty, J-Y., Incipient Metals: Functional Materials with a Unique Bonding Mechanism. *Adv. Mater*. **2018**, *30* (52), 1803777.
(40) Guarneri, L.; Jakobs, S.; Hoegen, A.; Maier, S.; Xu, M.; Zhu, M.; Wahl, S.; Teichrib, C.; Zhou, Y.; Cojocaru-Mirédin, O.; Raghuwanshi, M.; SchÖn, C-F.; DrÖgeler, M.; Stampfer, C.; Lobo, R, P, S.; Piarristeguy, A.; Pradel, A.; Raty, J-Y.; Wuttig, M., Metavalent Bonding in Crystalline Solids: How Does It Collapse?. *Adv. Mater*. **2021**, *33* (39) 2102356.
(41) Yu, Y.; Cagnoni, M.; Cojocaru-Mirédin, O.; Wuttig, M.; Chalcogenide Thermoelectrics Empowered by an Unconventional Bonding Mechanism. *Adv. Funct. Mater*. **2020**, *30* (8), 1904862.
(42) Cheng, Y.; Cojocaru-Mirédin, O.; Keutgen, Jens.; Yu, Y.; Küpers, M.; Schumacher, M.; Golub, P.; Raty, J-Y.; Dronskowski, R.; Wuttig, M.; Understanding the Structure and Properties of Sesqui-Chalcogenides (i.e., V_2VI_3 or Pn_2Ch_3 (Pn = Pnictogen, Ch = Chalcogen) Compounds) from a Bonding Perspective. *Adv. Mater*. **2019**, 31 (43), 1904316.
(43) Sarkar, D.; Roychowdhury, S.; Arora, R.; Ghosh, T.; Vasdev, A.; Joseph, B.; Sheet, G.; Waghmare, U, V.; Biawas, K., Metavalent Bonding in GeSe Leads to High Thermoelectric Performance, *Angew. Chem.* **2021**, *133* (18), 10438-10446.
(44) An, D.; Wang, J.; Zhang, J.; Zhai, X.; Kang, Z.; Fan, W.; Yan, J.; Liu, Y.; Lu, L.; Jia, C-L.; Wuttig, M.; Cojocaru-Mirédin, O.; Chen, S.; Wang, W.; Snyder, G. J.; Yu, Y.; Retarding Ostwald ripening through Gibbs adsorption and interfacial complexions leads to high-performance SnTe thermoelectrics. *Energy Environ. Sci*. **2021**, *14*, 5469-5479.
(45) Luo, Y.; Yang, J.; Li, G.; Liu, M.; Xiao, Y.; Fu, L.; Li, W.; Zhu, P.; Peng, J.; Gao, S.; Zhang, J., Enhancement of the thermoelectric performance of polycrystalline $In_4Se_{2.5}$ by copper intercalation and bromine substitution. *Adv. Energy Mater.* **2014,** *4* (2), 1300599.
(46) Shuai, J., Kim, H-S.; Lan, Y.; Chen, S.; Liu, Y.; Zhao, H.; Sui, J.; Ren, Z.; Study on thermoelectric performance by Na doping in nanostructured $Mg_{1-x}Na_xAg_{0.97}Sb_{0.99.}$ Nano Energy **2015**, *11*, 640-646.
(47) Kim, H.-S.; Gibbs, Z. M.; Tang, Y.; Wang, H.; Snyder, G. J., Characterization of Lorenz number with Seebeck coefficient measurement. *APL Mater.* **2015,** *3* (4), 041506.
(48) Liu, Z-Y.; Zhu, J-L.; Tong, X.; Niu, S.; Zhao, W-Y., A review of $CoSb_3$-based skutterudite thermoelectric materials. *J. Adv. Ceram.* **2020**, *9*, 647-673.
(49) Tan, G.; Shi, F.; Doak, J. W.; Sun, H.; Zhao, L.-D.; Wang, P.; Uher, C.; Wolverton, C.; Dravid, V. P.; Kanatzidis, M. G., Extraordinary role of Hg in enhancing the thermoelectric performance of p-type SnTe. *Energy Environ. Sci.* **2015,** *8* (1), 267-277.
(50) Pang, H.; Qiu, Y.; Wang, D.; Qin, Y.; Huang, R.; Yang, Z.; Zhang, X.; Zhao, L-D.; Realizing N-type SnTe Thermoelectrics with Competitive Performance through Suppressing Sn Vacancies. *J. Am. Chem. Soc.* **2021**, *143* (23), 8538–8542.
(51) Xiao, Y.; Wang, D.; Zhang, Y.; Chen, C.; Zhang, S.; Wang, K.; Wang, G.; Pennycook, S. J.; Snyder, G. J.; Wu, H., Band sharpening and band alignment enable high quality factor to enhance thermoelectric performance in n-type PbS. *J. Am. Chem. Soc.* **2020,** *142* (8), 4051-4060.
(52) Qin, Y.; Hong, T.; Qin, B.; Wang, D.; He, W.; Gao, X.; Xiao, Y.; Zhao, L-D.; Contrasting Cu Roles Lead to High Ranged Thermoelectric Performance of PbS, *Adv. Funct. Mater*. **2021**, *31* (34), 2102185.
(53) Tan, G.; Zhang, X.; Hao, S.; Chi, H.; Bailey, T. P.; Su, X.; Uher, C.; Dravid, V. P.; Wolverton, C.; Kanatzidis, M. G., Enhanced density-of-states effective mass and strained endotaxial nanostructures in Sb-doped $Pb_{0.97}Cd_{0.03}Te$ thermoelectric alloys. *ACS Appl. Mater. Inter.* **2019,** *11* (9), 9197-9204.

(54) Luo, Z.-Z.; Cai, S.; Hao, S.; Bailey, T. P.; Luo, Y.; Luo, W.; Yu, Y.; Uher, C.; Wolverton, C.; Dravid, V. P.; Zou, Z.; Yan, Q.; Kanatzidis, M. G.; Extrodinary role of Zn in enhancing thermoelectric performance of Ga-doped n-type PbTe. Energy Environ. Sci., **2022**, DOI: 10.1039/D1EE02986J.
(55) Zhu, T.; Fu, C.; Xie, H.; Liu, Y.; Zhao, X., High efficiency half-Heusler thermoelectric materials for energy harvesting. *Adv. Energy Mater.* **2015,** *5* (19), 1500588.
(56) Zhu, T.; Yu, G.; Xu, J.; Wu, H.; Fu, C.; Liu, X.; He, J.; Zhao, X., The Role of Electron–Phonon Interaction in Heavily Doped Fine-Grained Bulk Silicons as Thermoelectric Materials. *Adv. Electron. Mater.* **2016,** *2* (8), 1600171.
(57) Cai, S.; Hao, S.; Luo, Y.; Su, X.; Luo, Z.-Z.; Hu, X.; Wolverton, C.; Dravid, V. P.; Kanatzidis, M. G., Ultralow Thermal Conductivity and Thermoelectric Properties of $Rb_2Bi_8Se_{13}$. *Chem. Mater.,* **2020,** *32* (8), 3561-3569.
(58) Tan, G.; Hao, S.; Zhao, J.; Wolverton, C.; Kanatzidis, M. G., High thermoelectric performance in electron-doped $AgBi_3S_5$ with ultralow thermal conductivity. *J. Am. Chem. Soc.* **2017,** *139* (18), 6467-6473.
(59) Li, W.; Lin, S.; Weiss, M.; Chen, Z.; Li, J.; Xu, Y.; Zeier, W. G.; Pei, Y., Crystal structure induced ultralow lattice thermal conductivity in thermoelectric Ag_9AlSe_6. *Adv. Energy Mater.* **2018,** *8* (18), 1800030.
(60) Lim, Y. S.; Song, M.; Lee, S.; An, T.-H.; Park, C.; Seo, W.-S., Enhanced thermoelectric properties and their controllability in p-type $(BiSb)_2Te_3$ compounds through simultaneous adjustment of charge and thermal transports by Cu incorporation. *J. Alloys Compd.* **2016,** *687*, 320-325.
(61) Nolas, G. S.; Sharp, J.; Goldsmid, H. J., Low-Dimensional Thermoelectric Materials. In *Thermoelectrics*, Springer: 2001; pp 235-254.
(62) Luo, Y.; Cai, S.; Hua, X.; Chen, H.; Liang, Q.; Du, C.; Zheng, Y.; Shen, J.; Xu, J.; Wolverton, C.; Dravid, V. P.; Yan, Q.; Kanatzidis, M. G., High thermoelectric performance in polycrystalline SnSe via dual-doping with Ag/Na and nanostructuring with Ag_8SnSe_6. Adv. Energy Mater. **2019**, *9*(2), 1803072.
(63) Wu, C.-F.; Wei, T.-R.; Li, J.-F., Enhancing average ZT in pristine PbSe by over-stoichiometric Pb addition. *APL Mater.* **2016,** *4* (10), 104801.
(64) Zhao, L.-D.; Zhang, X.; Wu, H.; Tan, G.; Pei, Y.; Xiao, Y.; Chang, C.; Wu, D.; Chi, H.; Zheng, L., Enhanced thermoelectric properties in the counter-doped SnTe system with strained endotaxial SrTe. *J. Am. Chem. Soc.* **2016,** *138* (7), 2366-2373.
(65) Huang, L.-F.; Zeng, Z., Roles of mass, structure, and bond strength in the phonon properties and lattice anharmonicity of single-layer Mo and W dichalcogenides. *J. Phys. Chem. C* **2015,** *119* (32), 18779-18789.
(66) Hao, S.; Ward, L.; Luo, Z-Z.; Ozolins, Vidvuds, Dravid, V. P.; Kanatzidis, M. G.; Wolverton, C., Computational prediction of high thermoelectric performance in hole doped layered GeSe. *Chem. Mater.* **2019,** *31* (8), 3018-3024.
(67) Zhang, Y.; Skoug, E.; Cain, J.; Ozoliņš, V.; Morelli, D.; Wolverton, C., First-principles description of anomalously low lattice thermal conductivity in thermoelectric Cu-Sb-Se ternary semiconductors. *Phys. Rev. B* **2012,** *85* (5), 054306.
(68) Hao, S.; Shi, F.; Dravid, V. P.; Kanatzidis, M. G.; Wolverton, C., Computational prediction of high thermoelectric performance in hole doped layered GeSe. *Chem. Mater.* **2016,** *28* (9), 3218-3226.

Figure captions

Figure 1. Crystal structures of $Bi_2Si_2Te_6$ along the *a*-axis (a) and *c*-axis (b). (c) Rietveld refinement of the powder XRD pattern of $Bi_2Si_2Te_6$ powders prepared by ball-milling and annealing. (d) Electronic band structures of $Bi_2Si_2Te_6$. (e) Powder XRD patterns of $Bi_{2-x}Pb_xSi_2Te_6$ (x = 0, 0.01, 0.02, 0.03, and 0.04).

Figure 2. FESEM images of (a, d) $Bi_2Si_2Te_6$, (b, e) $Bi_{1.98}Pb_{0.02}Si_2Te_6$, and (c, f) $Bi_{1.96}Pb_{0.04}Si_2Te_6$ pellets.

Figure 3. STEM annular bright field (ABF) image (a) and corresponding EDXS profiles of $Bi_{1.96}Pb_{0.04}Si_2Te_6$ (b), TEM images (c, d), corresponding selected area electron diffraction (e) and high-resolution TEM images (f, g) of $Bi_{1.96}Pb_{0.04}Si_2Te_6$.

Figure 4. Temperature-dependent (a) electrical conductivities, (b) Seebeck coefficients, (c) power factors, (d) thermal conductivities, (e) lattice thermal conductivities, and (f) ZT values of $Bi_{2-x}Pb_xSi_2Te_6$ (x = 0, 0.01, 0.02, 0.03, and 0.04).

Figure 5. (a) Phonon dispersions, (b) projected phonon density of states (PDOS), (c) Grüneisen dispersion spectrum, and (d) calculated lattice thermal conductivities ($\kappa_{Latt.}$) in the *a*-, *b*-, and *c*-axes of $Bi_2Si_2Te_6$ and its average lattice thermal conductivity. The TA, TA′ and LA modes are plotted as red, green and blue respectively in panel a and c.

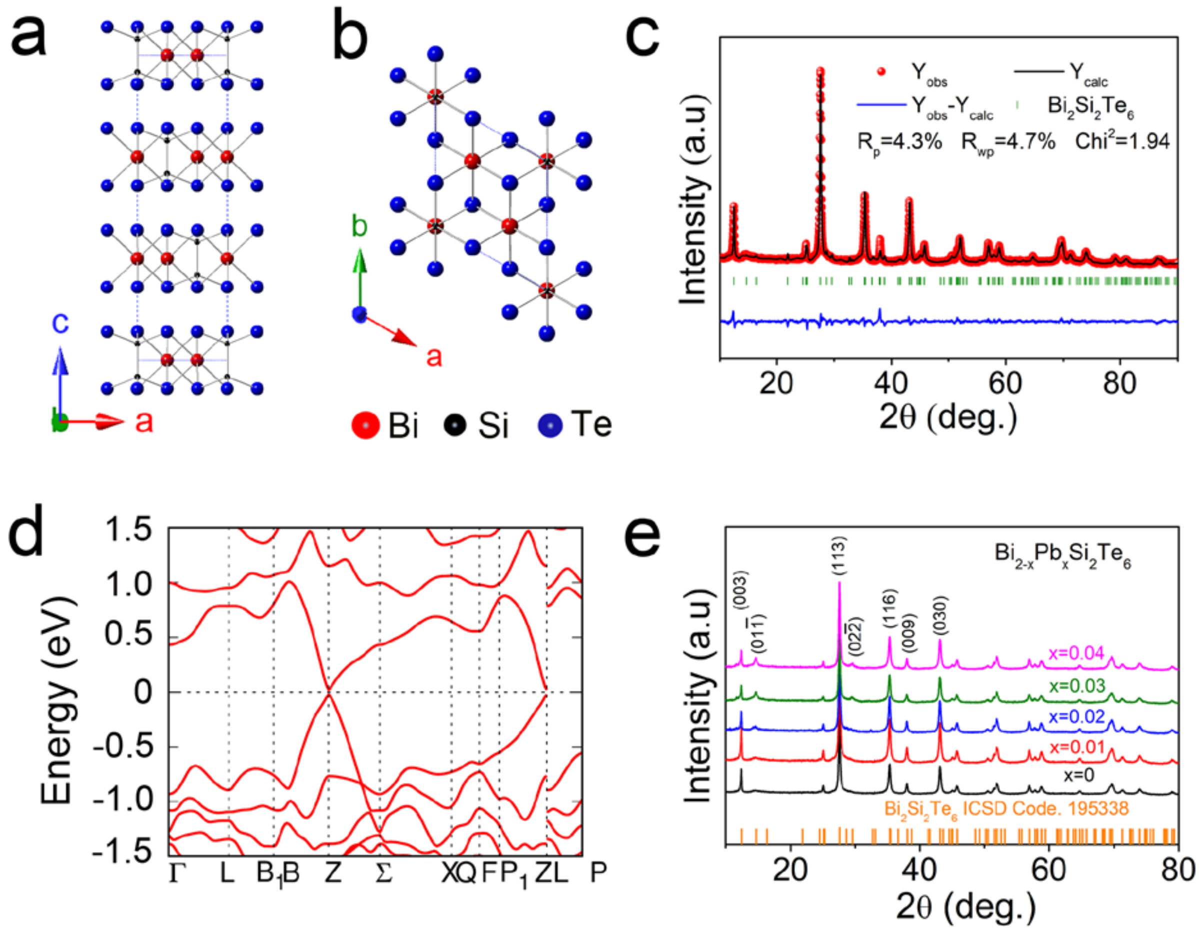

Figure 1. Crystal structures of $Bi_2Si_2Te_6$ along the *a*-axis (a) and *c*-axis (b). (c) Rietveld refinement of the powder XRD pattern of $Bi_2Si_2Te_6$ powders prepared by ball-milling and annealing. (d) Electronic band structures of $Bi_2Si_2Te_6$. (e) Powder XRD patterns of $Bi_{2-x}Pb_xSi_2Te_6$ (x = 0, 0.01, 0.02, 0.03, and 0.04).

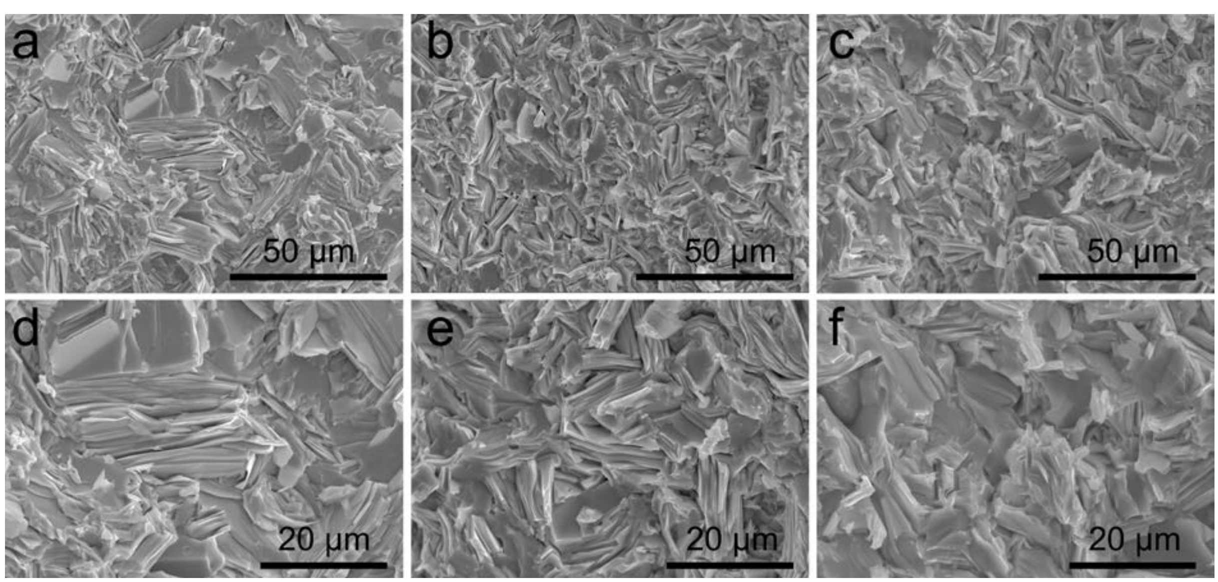

Figure 2. FESEM images of (a, d) $Bi_2Si_2Te_6$, (b, e) $Bi_{1.98}Pb_{0.02}Si_2Te_6$, and (c, f) $Bi_{1.96}Pb_{0.04}Si_2Te_6$ pellets.

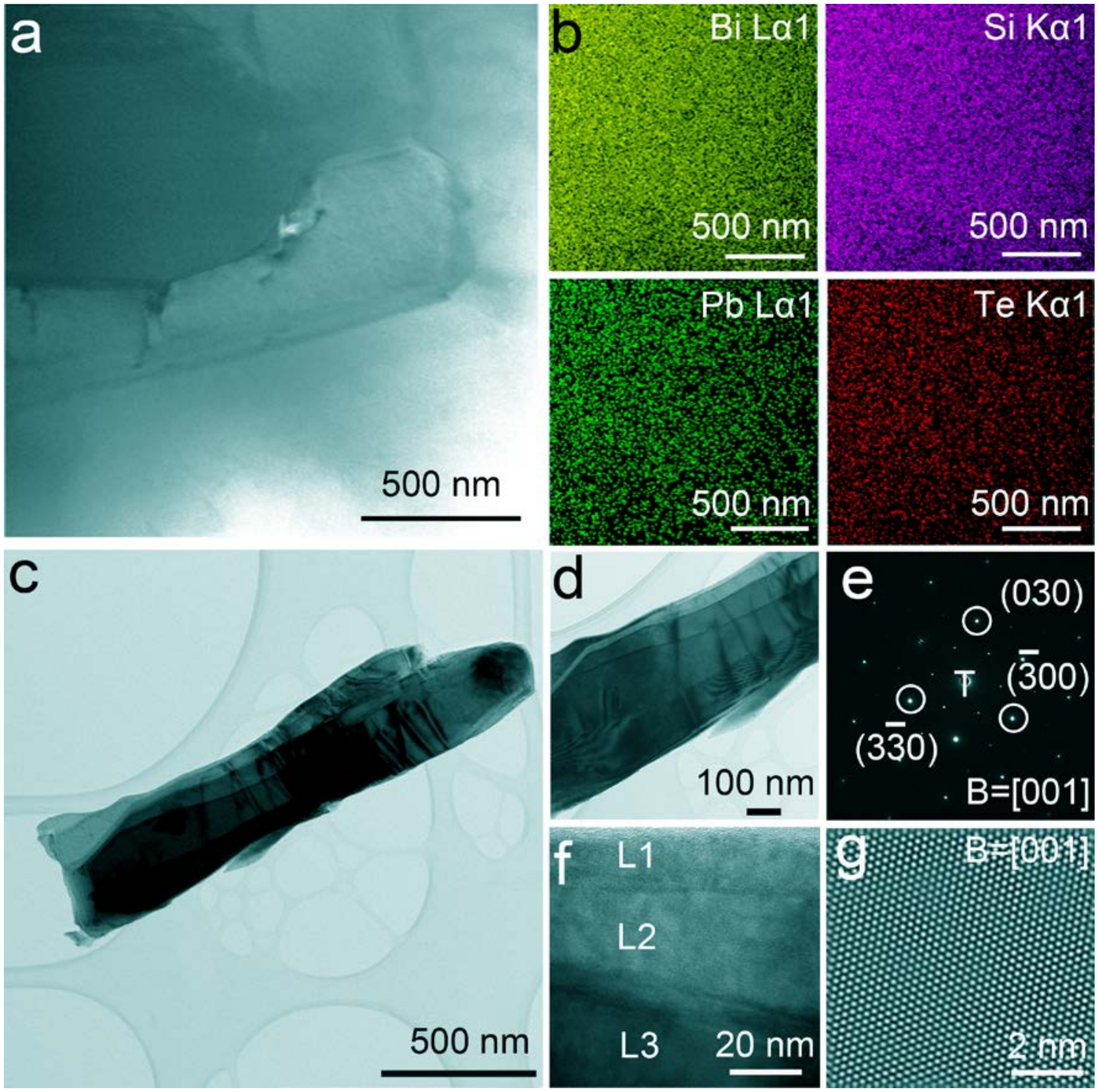

Figure 3. STEM annular bright field (ABF) image (a) and corresponding EDXS profiles of $Bi_{1.96}Pb_{0.04}Si_2Te_6$ (b), TEM images (c, d), corresponding selected area electron diffraction (e) and high-resolution TEM images (f, g) of $Bi_{1.96}Pb_{0.04}Si_2Te_6$.

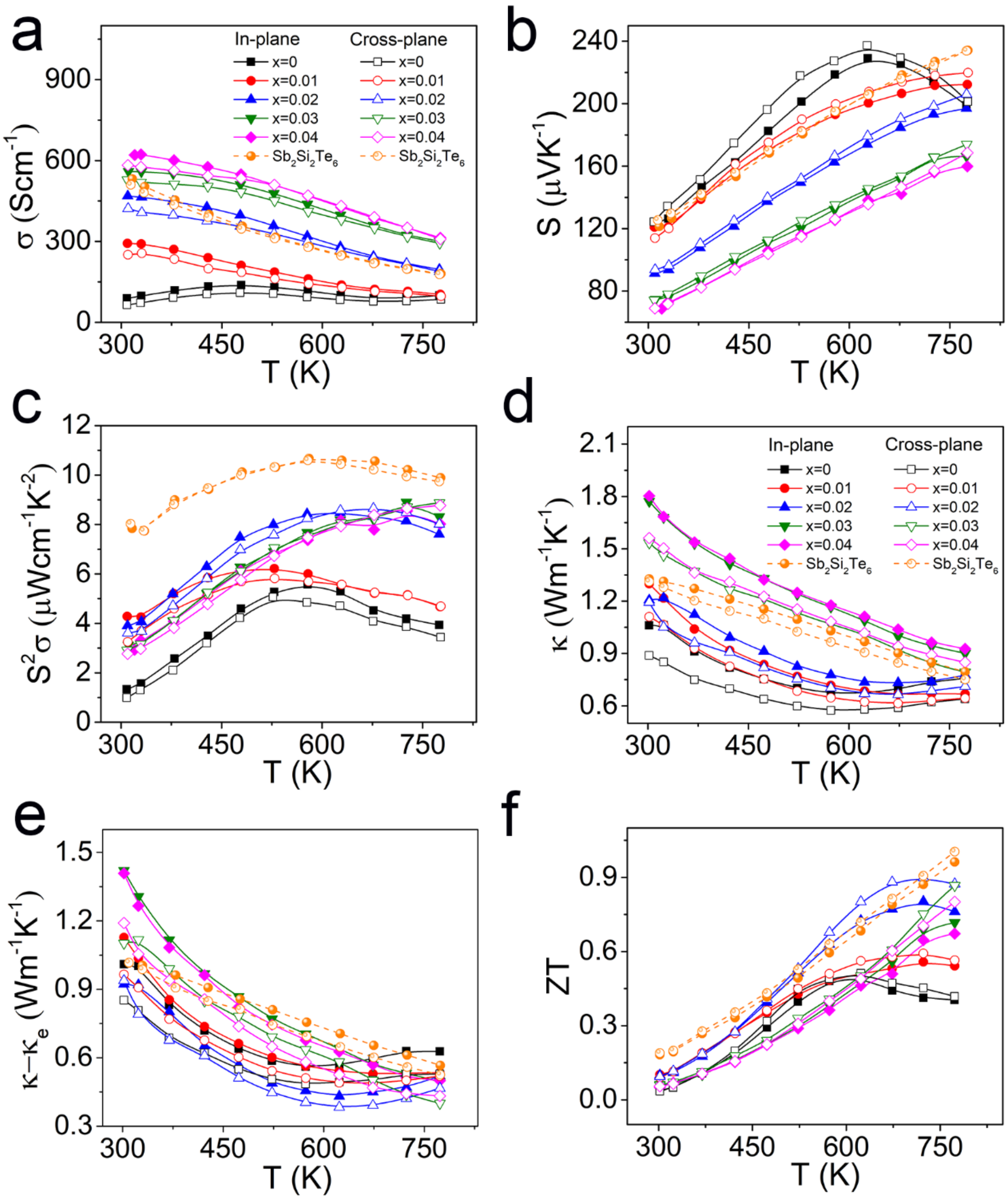

Figure 4. Temperature-dependent (a) electrical conductivities, (b) Seebeck coefficients, (c) power factors, (d) thermal conductivities, (e) lattice thermal conductivities, and (f) ZT values of $Bi_{2-x}Pb_xSi_2Te_6$ (x = 0, 0.01, 0.02, 0.03, and 0.04).

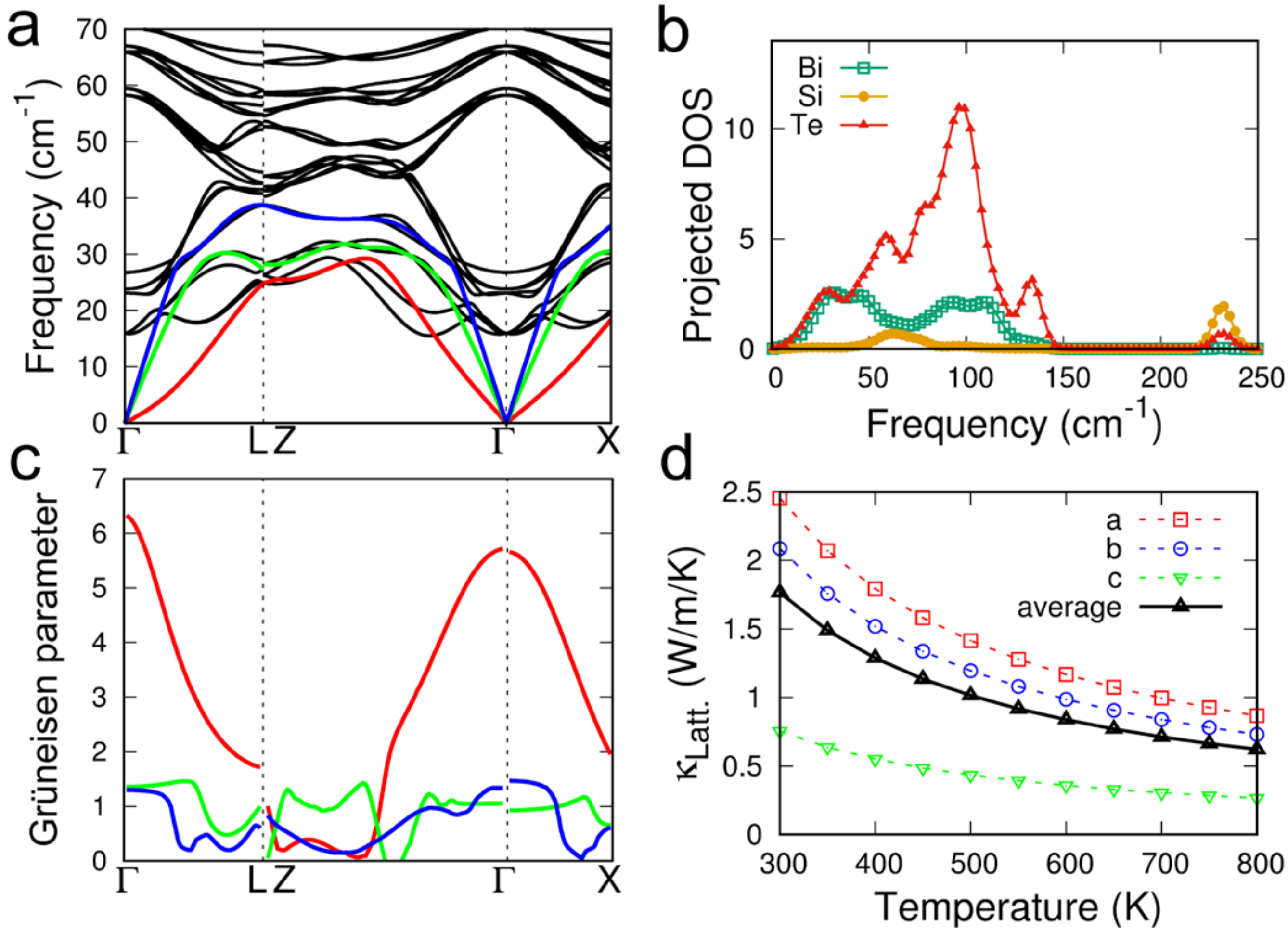

Figure 5. (a) Phonon dispersions, (b) projected phonon density of states (PDOS), (c) Grüneisen dispersion spectrum, and (d) calculated lattice thermal conductivities ($\kappa_{Latt.}$) in the *a*-, *b*-, and *c*-axes of $Bi_2Si_2Te_6$ and its average lattice thermal conductivity. The TA, TA′ and LA modes are plotted as red, green and blue respectively in panel a and c.

ToC Graphic

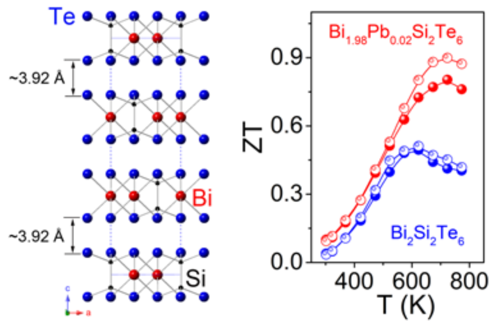

Te
~3.92 Å
~3.92 Å
Bi
Si
Bi1.98Pb0.02Si2Te6
Bi2Si2Te6
ZT
0.0
0.3
0.6
0.9
400
600
800
T (K)